Electronic Supplementary Information

Benzophenone-containing phosphors with unprecedented long lifetime of 1.8 s under ambient conditions

Yuming Su, [a,b] Minjian Wu, [b] Guangming Wang, [b] Jiuyang Li, [b] Xuefeng Chen, [b] Xun Li, [b] Guoxiang Wang,*[a] and Kaka Zhang*[b]

[a.] *School of Chemistry and Chemical Engineering, Hunan Institute of Science and Technology, People's Republic of China.*
[b.] *Key Laboratory of Synthetic and Self-Assembly Chemistry for Organic Functional Molecules, Shanghai Institute of Organic Chemistry, University of Chinese Academy of Sciences, Chinese Academy of Sciences, 345 Lingling Road, Shanghai 200032, People's Republic of China.*

E-mail: 11991397@hnist.edu.cn; zhangkaka@sioc.ac.cn.

Table of Contents

Materials

Benzophenone (compound **1**, 99%, Mackny), 4-methoxybenzophenone (compound **2**, MeOBP) (99%, Innochem), 4-benzoylbiphenyl (compound **3**, 99%, Anage), (4-bromophenyl)(phenyl)methanone (99.6%, Bide Pharmatech), 2-naphthaleneboronic acid (99%, Bide Pharmatech), 4-methoxyphenylboronic acid (99%, Admas), 4-biphenylboronic acid (99%, Bide Pharmatech), potassium carbonate (AR, Shanghai Dahe Chemicals Co., Ltd.), palladium(II) acetate (99% Pd 46.0-48.0%, Innochem), N,N-dimethyformamide (AR, Shanghai Experimental Reagent Co., Ltd.), deuterium oxide (D_2O) (99.8%, Admas), Pd/C (Sigma-Aldrich), phenyl benzoate (PhB) (99%, Energy Chemical), rhodamine 6G (Biological stain, Aladdin).

Synthesis of compound 4 via Suzuki coupling

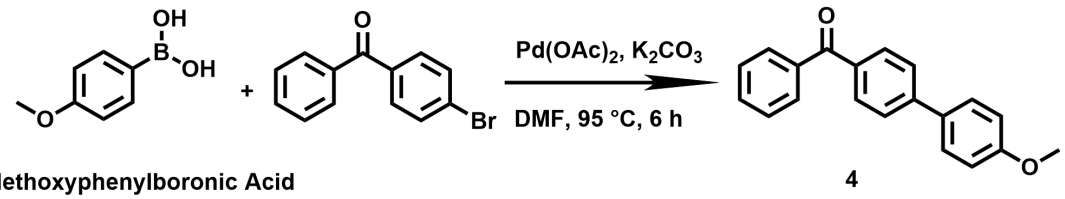

4-Methoxyphenylboronic Acid

4

Into a round bottom flask were added 4-methoxyphenylboronic acid (84 mg, 0.55 mmol), (4-bromophenyl)(phenyl)methanone (131 mg, 0.5 mmol), palladium(II) acetate (1.1 mg, 0.005 mmol), potassium carbonate (138 mg, 1 mmol) and N,N-dimethyformamide (6 mL). The reaction mixture was stirred at 95 °C for 6 hours. After reaction, excess water was added to the reaction mixture, leading to the precipitation of crude product. After filtration and washing by water, N,N-dimethyformamide was removed. The crude product was dissolved with dichloromethane, dried with anhydrous sodium sulfate, and concentrated by rotary evaporation. The crude product was purified by column chromatography over silica gel using petroleum ether/dichloromethane (1:1) to give compound **4** (103 mg, 71%). The compound **4** was further purified by three cycles of recrystallization in spectroscopic grade dichloromethane/hexane. ^{1}H NMR (400 MHz, Chloroform-d) δ

7.96 – 7.84 (m, 2H), 7.84 – 7.75 (m, 2H), 7.70 – 7.62 (m, 2H), 7.60 (d, J = 2.1 Hz, 1H), 7.60 – 7.55 (m, 2H), 7.49 (tt, J = 6.8, 1.4 Hz, 2H), 7.08 – 6.89 (m, 2H), 3.86 (s, 3H). HRMS m/z found (calcd for $C_{20}H_{17}O_2^+$): 289.1232 (289.1224).

Synthesis of compound 5 via Suzuki coupling

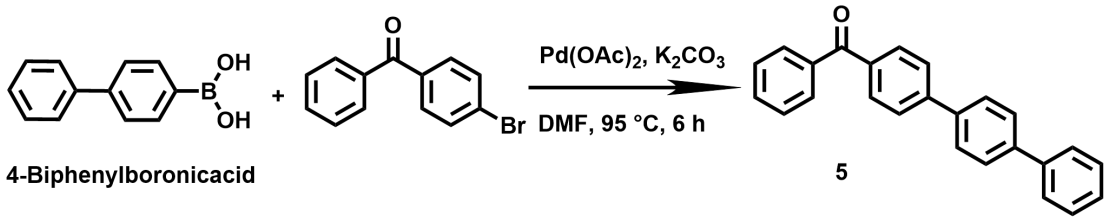

4-Biphenylboronicacid **5**

Into a round bottom flask were added 4-biphenylboronic acid (109 mg, 0.55 mmol), (4-bromophenyl)(phenyl)methanone (131 mg, 0.5 mmol), palladium(II) acetate (1.1 mg, 0.005 mmol), potassium carbonate (138 mg, 1 mmol) and N,N-dimethyformamide (6 mL). The reaction mixture was stirred at 95 °C for 6 hours. After reaction, excess water was added to the reaction mixture, leading to the precipitation of crude product. After filtration and washing by water, N,N-dimethyformamide was removed. The crude product was dissolved with dichloromethane, dried with anhydrous sodium sulfate, and concentrated by rotary evaporation. The crude product was purified by column chromatography over silica gel using petroleum ether/dichloromethane (1:1) to give white compound **5** (159 mg, 95%). The compound **5** was further purified by two cycles of recrystallization in spectroscopic grade dichloromethane/hexane. ^{1}H NMR (400 MHz, Chloroform-d) δ 7.94 – 7.87 (m, 2H), 7.84 (dt, J = 7.0, 1.4 Hz, 2H), 7.76 (d, J = 1.9 Hz, 1H), 7.74 (d, J = 1.9 Hz, 1H), 7.73 (s, 2H), 7.72 – 7.68 (m, 2H), 7.68 – 7.63 (m, 2H), 7.63 – 7.56 (m, 1H), 7.53 – 7.43 (m, 4H), 7.42 – 7.32 (m, 1H). HRMS m/z found (calcd for $C_{25}H_{19}O^+$): 335.1442 (335.1431).

Synthesis of compound 6 via Suzuki coupling

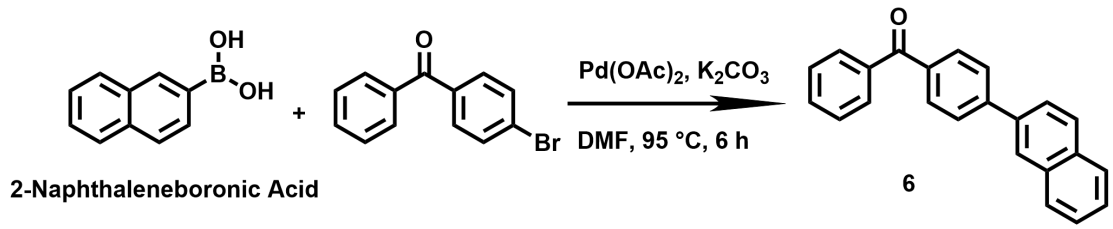

Into a round bottom flask were added 2-naphthaleneboronic acid (361 mg, 2.1 mmol), (4-bromophenyl)(phenyl)methanone (522 mg, 2 mmol), palladium(II) acetate (4.48 mg, 0.02 mmol), potassium carbonate (552 mg, 4 mmol) and N,N-dimethyformamide (12 mL). The reaction mixture was stirred at 95 °C for 6 hours. After reaction, excess water was added to the reaction mixture, leading to the precipitation of crude product. After filtration and washing by water, N,N-dimethyformamide was removed. The crude product was dissolved with dichloromethane, dried with anhydrous sodium sulfate, and concentrated by rotary evaporation. The crude product was purified by column chromatography over silica gel using petroleum ether/dichloromethane (1:1) to give white compound **6** (479 mg, 78%). The compound **6** was further purified by two cycles of recrystallization in spectroscopic grade dichloromethane/hexane. ^{1}H NMR (400 MHz, Chloroform-d) δ 8.11 (d, J = 1.9 Hz, 1H), 7.99 – 7.93 (m, 2H), 7.93 – 7.90 (m, 2H), 7.90 – 7.85 (m, 2H), 7.84 (d, J = 1.9 Hz, 2H), 7.83 – 7.74 (m, 2H), 7.65 – 7.56 (m, 1H), 7.53 (dd, J = 3.6, 2.2 Hz, 2H), 7.50 (dd, J = 7.2, 1.9 Hz, 2H). ^{13}C NMR (101 MHz, Chloroform-*d*) δ 196.47, 145.25, 137.88, 137.36, 136.37, 133.68, 133.11, 132.51, 130.92, 130.13, 128.84, 128.47, 128.44, 127.81, 127.32, 126.67, 126.58, 126.50, 125.34. HRMS m/z found (calcd for $C_{23}H_{17}O^{+}$): 309.1287 (309.1274). FT-IR (KBr, cm^{-1}): ν 3050.0, 1644.6, 1598.5, 1577.4, 1556.8, 1499.2, 1444.3, 1406.6, 1370.4, 1319.6, 1343.6, 1292.6, 1178.6, 1149.4, 1129.9, 1074.5, 1026.8, 1012.6, 999.2, 969.8, 938.3, 924.2, 896.1, 856.8, 841.6, 821.2, 795.0, 789.4, 751.3, 737.5, 730.0, 691.3, 666.0, 637.7, 623.4, 594.0, 541.0, 474.0, 466.4, 455.5.

Synthesis of deuterated compound 6

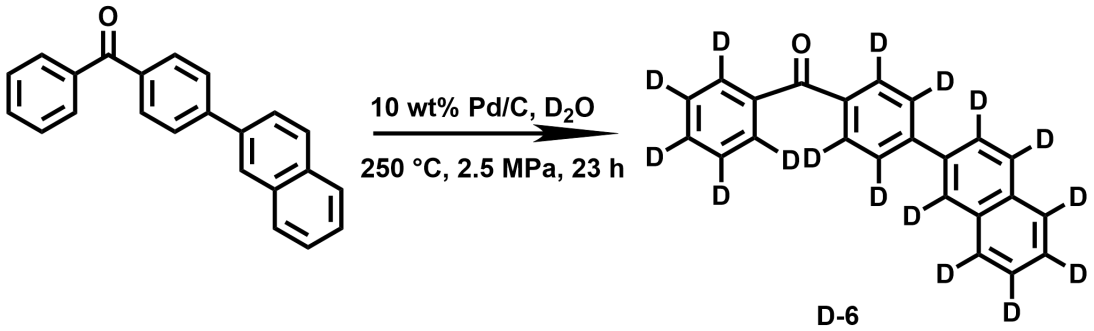

The undeuterated compound **6** (200 mg) was treated with 10 % Pd on active carbon (150 mg) and D_2O (26 mL) in a 0.13 L teflon-lined autoclave at 250 °C for 25 h. The internal pressure reached 2–2.5 MPa. The deuteration reaction was performed in a safe laboratory in our institute. After deuteration, the autoclave was cooled to room temperature. The D_2O phase of the reaction was washed three times with dichloromethane (50 mL each time). The crude product was dried on anhydrous sodium sulfate, concentrated by rotary evaporation. The crude product purified by column chromatography over silica gel using petroleum ether/dichloromethane (2:1) to give white powder (46.8 mg). The hydrogen atoms in compound **6** were randomly deuterated with a deuteration yield of 79%. ^{1}H NMR measurements using 1,4-dioxane as reference were used to estimate the deuteration yield.

Preparation of afterglow materials by doping compounds 1-6 into organic matrices

For the preparation of **6**-PhB materials, 500 μL compound **6** in dichloromethane (1 mg/mL) and 100 mg phenyl benzoate (PhB) were added into a 3 mL sample bottle, and then heated to 80 °C to give a molten mixture. Subsequently, the sample bottle was transferred to a bath of liquid nitrogen to immediately solidify the molten mixture. After standing at room temperature for tens of minutes, melt-cast materials were obtained. Melt-cast materials by using **1**-**5** dopants were prepared by similar procedures.

Physical measurements and instrumentation

Nuclear magnetic resonance (NMR) spectra were recorded on a JEOL Fourier-transform NMR spectrometer (400 MHz), including ^{1}H NMR and $^{13}C\{^{1}H\}$ NMR. Mass spectra were performed on Agilent Q-TOF 6520 liquid chromatograph mass spectrometer. FT-IR spectra were recorded on a Nicolet AVATAR-360 FT-IR spectrophotometer with a resolution of 4 cm^{-1}. UV-Vis absorption spectra were recorded on a Hitachi U-3310 UV-vis spectrophotometer and a Techcomp UV1050 UV-vis spectrophotometer. The steady-state and delayed emission spectra were collected by Hitachi FL-4700 fluorescence spectrometer equipped with chopping systems; the delayed emission spectra were obtained with a delay time of approximately 1 ms. The excited state decay profiles in millisecond to second region were collected by Hitachi FL-4700 fluorescence spectrometer equipped with chopping systems. Photographs and videos were captured by Apple iphone 11 cameras. Before imaging, samples were irradiated by a 365 nm UV lamp (5 W) for approximately 5 s at a distance of approximately 15 cm.

TD-DFT calculations

TD-DFT calculations were performed to study the photophysical properties of molecularly dispersed compounds **1**-**6** in PhB matrix. Since the afterglow properties are originated from the excited states of molecularly dispersed compounds **1**-**6** in the rigid PhB matrices where intermolecular rotation and vibration are largely restricted, the ground-state geometry of compounds **1**-**6** was used for all the TD-DFT calculations. The ground-state geometry of compounds **1**-**6** were optimized by a DFT calculation using B3LYP functional and 6-31G (d, p) basis set. The singlet excited states and triplet excited states were calculated on Gaussian 16 program (Revision A.03) with B3LYP functional and 6-31G (d, p) functional. Spin-orbit coupling (SOC) matrix elements between the singlet excited states and triplet excited states were calculated with spin-orbit mean-field (SOMF) methods on ORCA 4.2.1 program with B3LYP functional and def2-TZVP(-f) basis set. The obtained electronic structures were analyzed by Multiwfn software. All isosurface maps to show the electron

distribution and electronic transitions were rendered by Visual Molecular Dynamics (VMD) software based on the exported files from Multiwfn. (Neese F, *Wiley Interdiscip. Rev. Comput. Mol. Sci*. 2018, 8: 1327-1332; Becke AD, *Phys. Rev. A* 1988, 38: 3098-3100; Lee C, Yang W, Parr RG, *Phys. Rev. B.* 1988, 37: 785-789; Miehlich B, Savin A, Stoll H, Preuss H, *Chem. Phys. Lett.* 1989, 157: 200-206; Weigend F, Ahlrichs R, *Phys. Chem. Chem. Phys.* 2005, 7: 3297-3305; Lu T, Chen F, *J. Comput. Chem.* 2012, 33: 580-592; Humphrey W, Dalke A, Schulten K, *J. Mol. Graphics* 1996, 14: 33-38).

Table S1. Photophysical data of 1-6 compounds at room temperature.

Entry	λ_{abs} / nm	$\varepsilon \times 10^{-4}$ / $M^{-1}cm^{-1}$
1 in dichloromethane	253	1.62
1 in acetonitrile	251	1.51
1 in methanol	252	1.53
1 in chloroform	253	2.19
2 in dichloromethane	286(251)	1.99(1.39)
2 in acetonitrile	285(250)	1.63(0.97)
2 in methanol	287(251)	1.84(1.06)
2 in chloroform	287(253)	2.01(1.32)
3 in dichloromethane	290	2.38
3 in acetonitrile	290	2.80
3 in methanol	290	2.62
3 in chloroform	292	2.79
4 in dichloromethane	311(235)	2.1(1.9)
4 in acetonitrile	309	1.8
4 in methanol	312	1.9
4 in chloroform	313(246)	1.9(1.6)
5 in dichloromethane	309(255)	3.30(2.41)
5 in acetonitrile	309(255)	3.19(1.62)
5 in methanol	309(255)	3.39(2.02)
5 in chloroform	309(256)	3.07(3.02)
6 in dichloromethane	311(280)	3.5(4.0)
6 in acetonitrile	309(278)	3.4(3.7)
6 in methanol	310(278)	3.3(3.5)
6 in chloroform	311(282)	3.6(5.1)

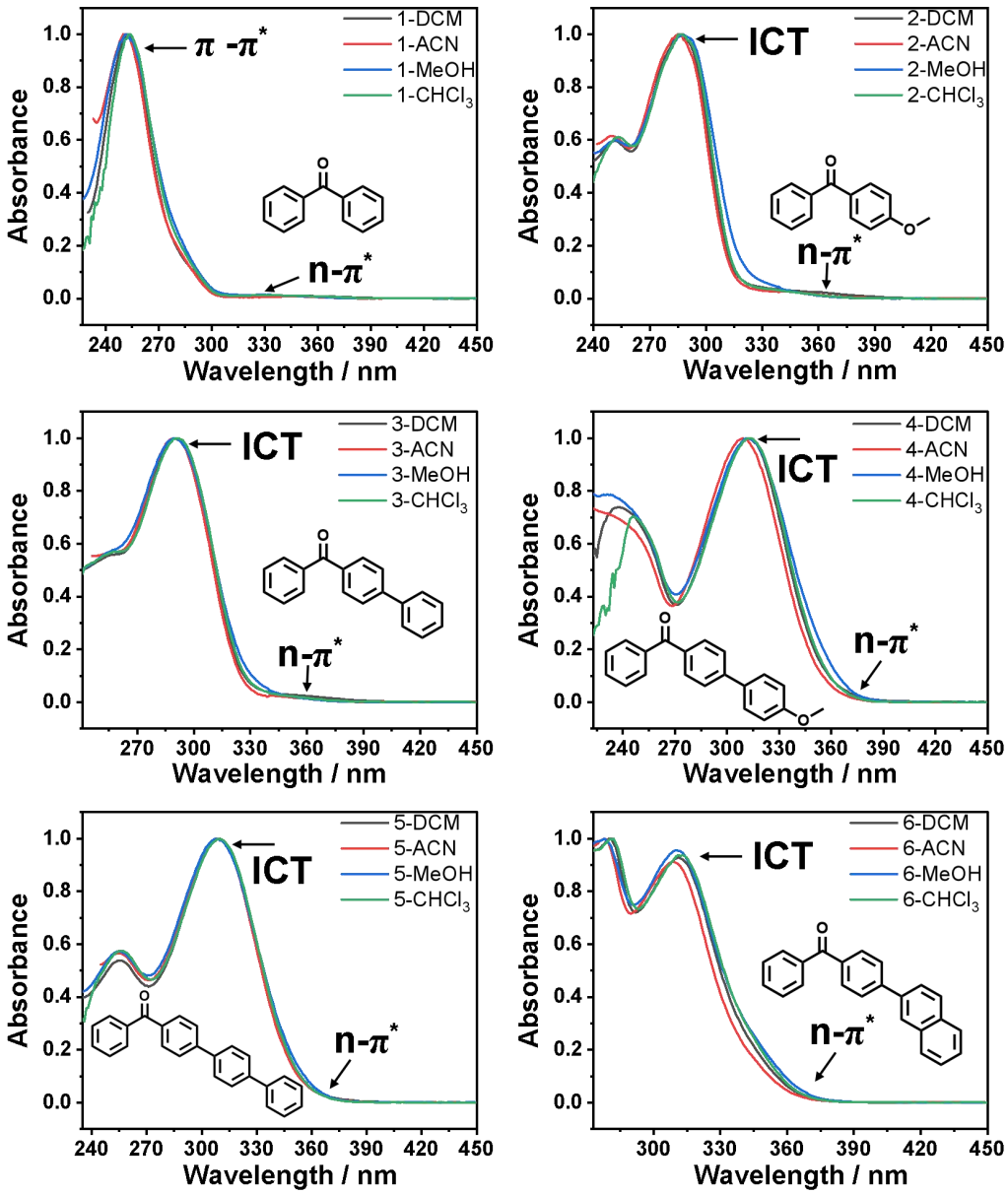

Figure S1. UV-vis spectra of compounds **1-6** in different solvents. DCM, ACN, MeOH and $CHCl_3$ refer to dichloromethane, acetonitrile, methanol and chloroform, respectively.

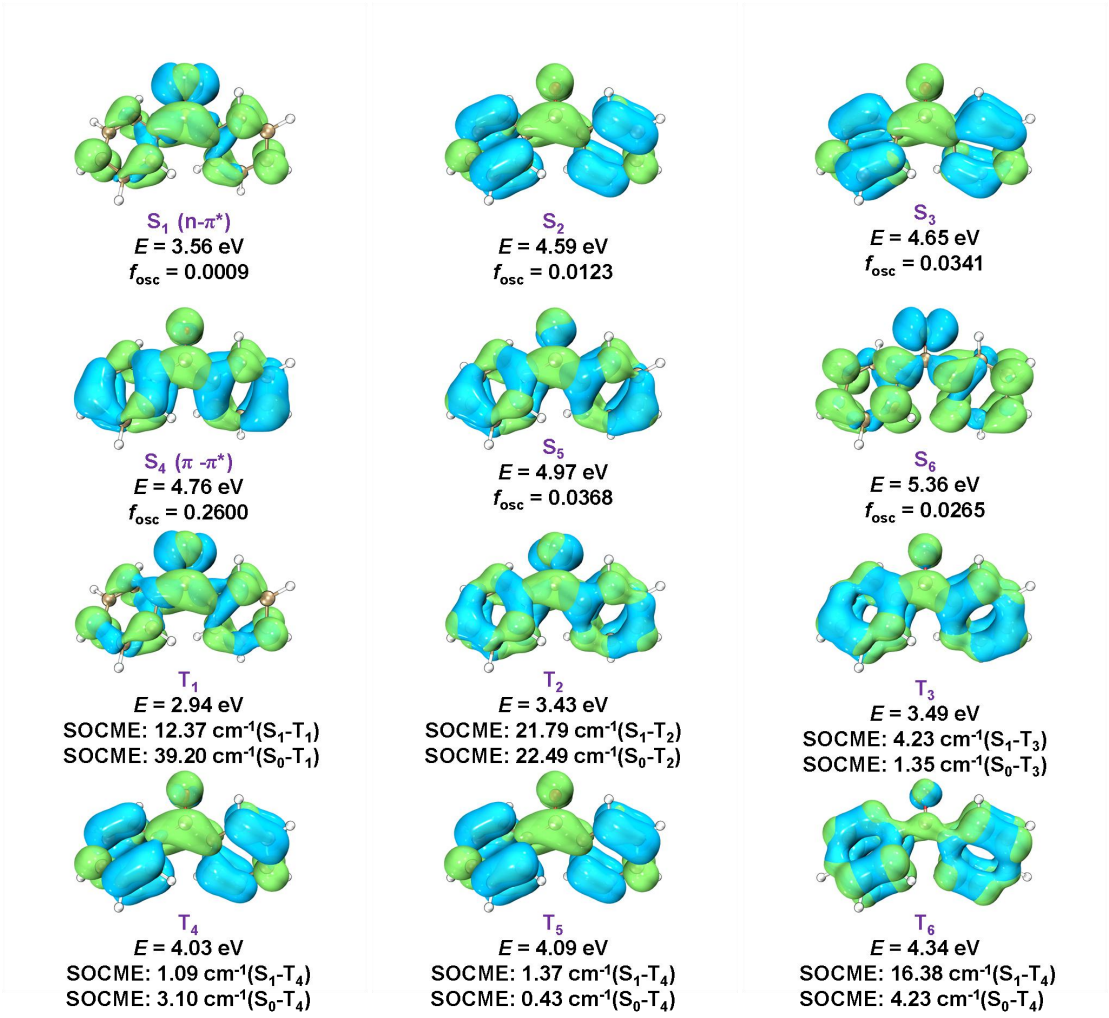

Figure S2. Iso-surface maps of electron-hole density difference of **1**'s S_n and T_n states, where blue and green iso-surfaces correspond to hole and electron distributions, respectively, and SOCME values. The ground-state geometry was optimized by a DFT calculation using B3LYP functional and 6-31G (d, p) basis set. The singlet excited states and triplet excited states were calculated on Gaussian 16 program (Revision A.03) with B3LYP functional and 6-31G (d, p) functional. Spin-orbit coupling (SOC) matrix elements between the singlet excited states and triplet excited states were calculated with spin-orbit mean-field (SOMF) methods on ORCA 4.2.1 program with B3LYP functional and def2-TZVP(-f) basis set.

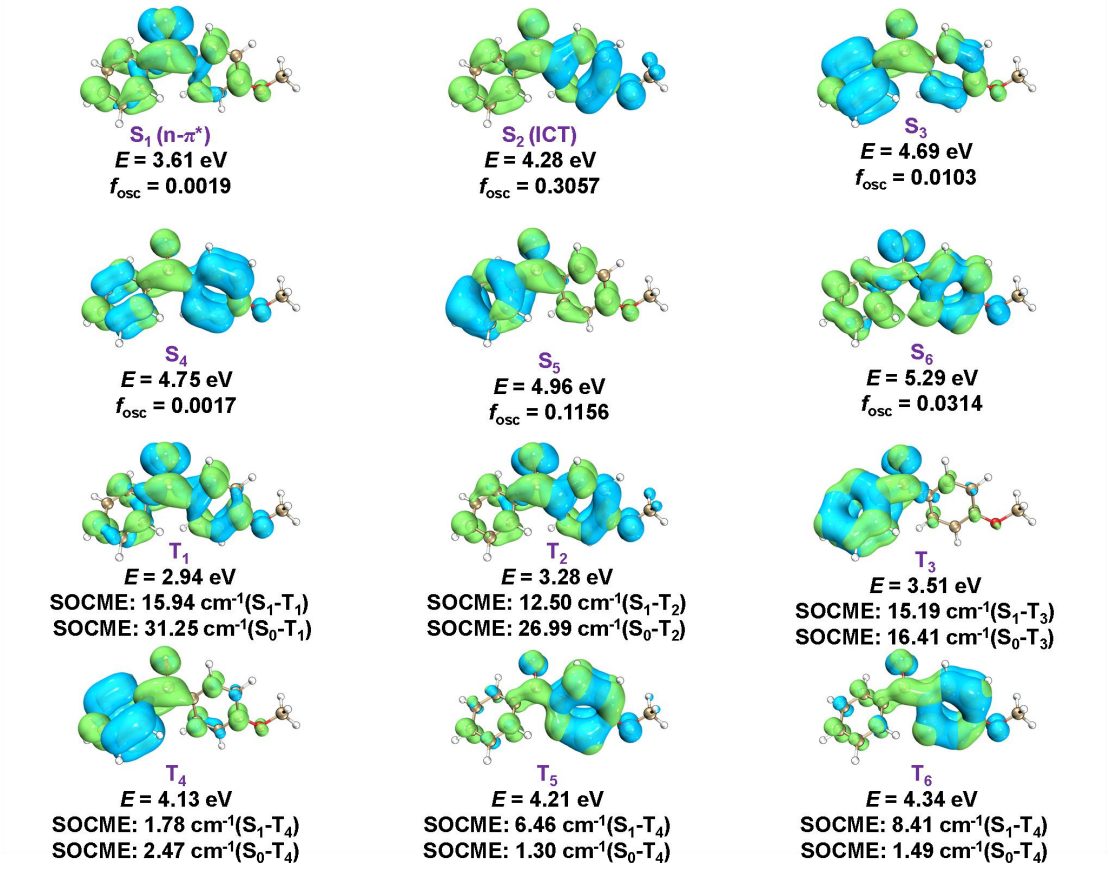

Figure S3. Iso-surface maps of electron-hole density difference of **2**'s S_n and T_n states, where blue and green iso-surfaces correspond to hole and electron distributions, respectively, and SOCME values. The ground-state geometry was optimized by a DFT calculation using B3LYP functional and 6-31G (d, p) basis set. The singlet excited states and triplet excited states were calculated on Gaussian 16 program (Revision A.03) with B3LYP functional and 6-31G (d, p) functional. Spin-orbit coupling (SOC) matrix elements between the singlet excited states and triplet excited states were calculated with spin-orbit mean-field (SOMF) methods on ORCA 4.2.1 program with B3LYP functional and def2-TZVP(-f) basis set.

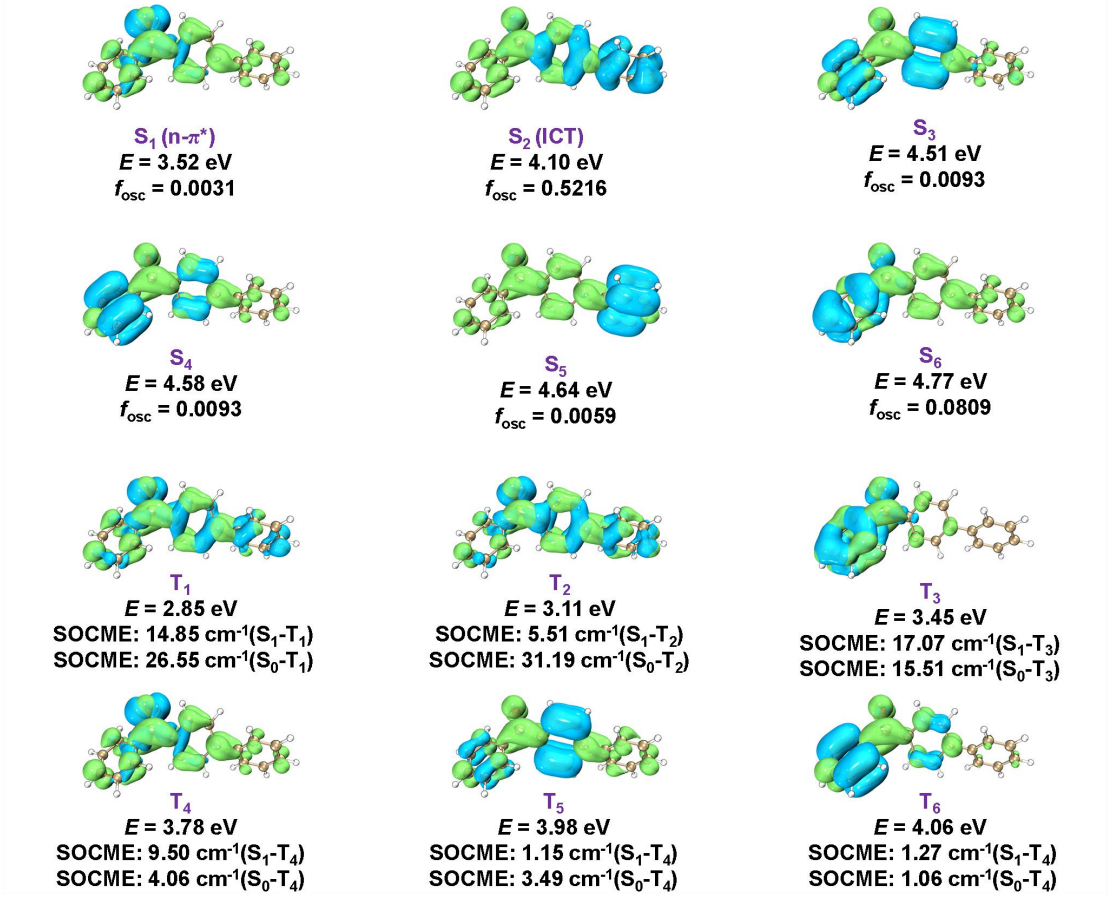

Figure S4. Iso-surface maps of electron-hole density difference of **3**'s S_n and T_n states, where blue and green iso-surfaces correspond to hole and electron distributions, respectively, and SOCME values. The ground-state geometry was optimized by a DFT calculation using B3LYP functional and 6-31G (d, p) basis set. The singlet excited states and triplet excited states were calculated on Gaussian 16 program (Revision A.03) with B3LYP functional and 6-31G (d, p) functional. Spin-orbit coupling (SOC) matrix elements between the singlet excited states and triplet excited states were calculated with spin-orbit mean-field (SOMF) methods on ORCA 4.2.1 program with B3LYP functional and def2-TZVP(-f) basis set.

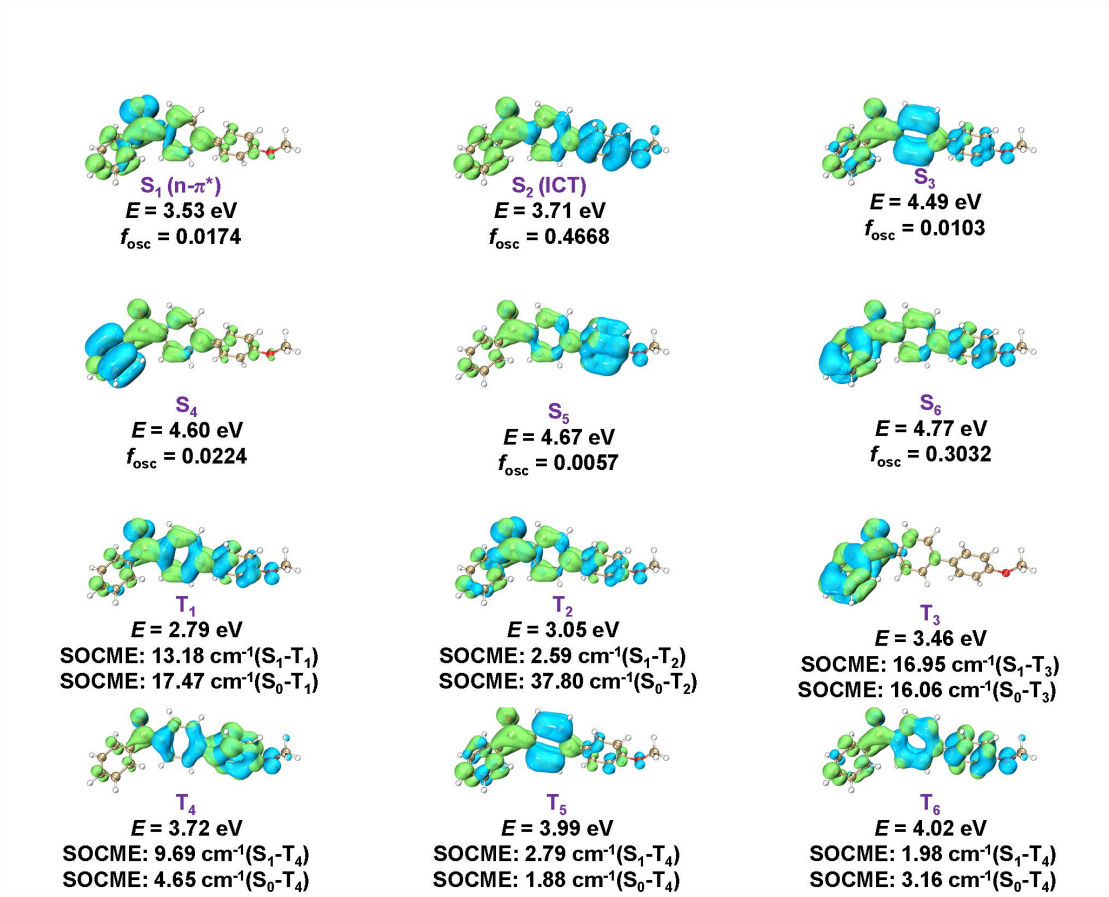

Figure S5. Iso-surface maps of electron-hole density difference of **4**'s S_n and T_n states, where blue and green iso-surfaces correspond to hole and electron distributions, respectively, and SOCME values. The ground-state geometry was optimized by a DFT calculation using B3LYP functional and 6-31G (d, p) basis set. The singlet excited states and triplet excited states were calculated on Gaussian 16 program (Revision A.03) with B3LYP functional and 6-31G (d, p) functional. Spin-orbit coupling (SOC) matrix elements between the singlet excited states and triplet excited states were calculated with spin-orbit mean-field (SOMF) methods on ORCA 4.2.1 program with B3LYP functional and def2-TZVP(-f) basis set.

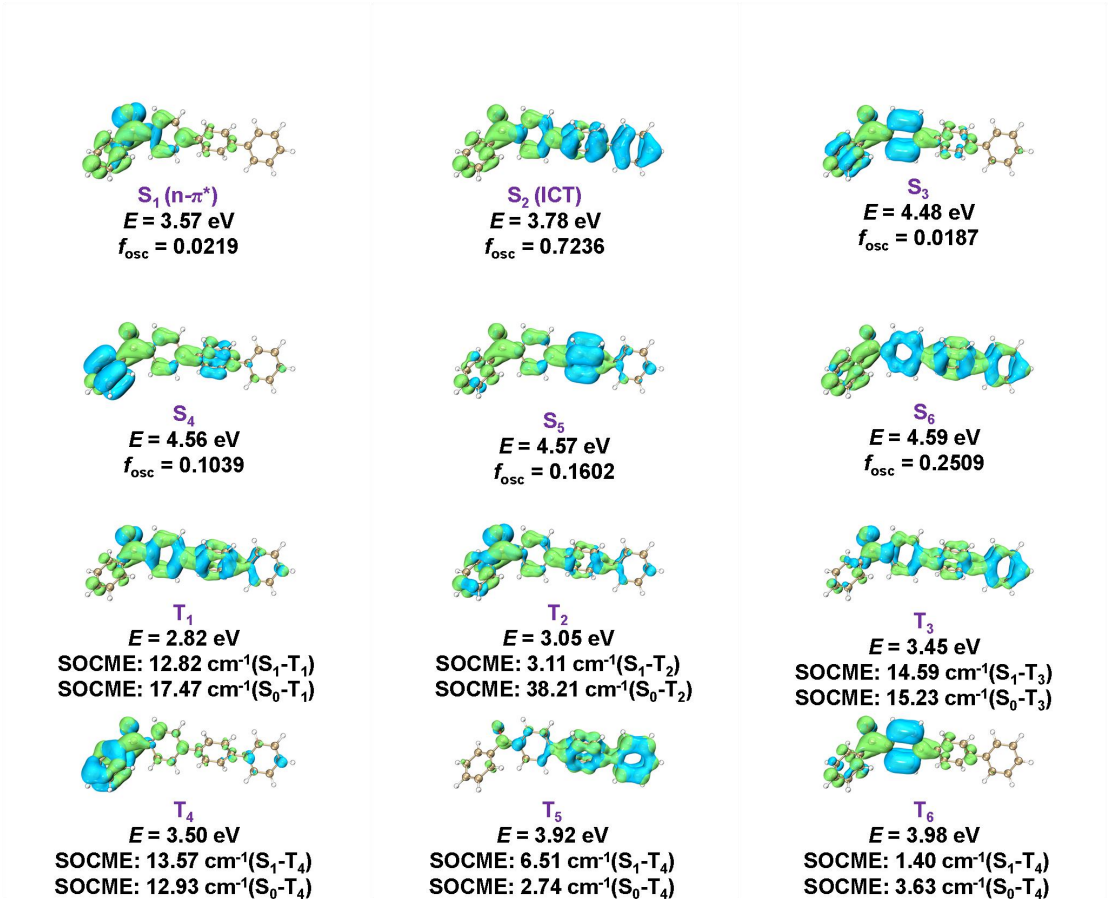

Figure S6. Iso-surface maps of electron-hole density difference of **5**'s S_n and T_n states, where blue and green iso-surfaces correspond to hole and electron distributions, respectively, and SOCME values. The ground-state geometry was optimized by a DFT calculation using B3LYP functional and 6-31G (d, p) basis set. The singlet excited states and triplet excited states were calculated on Gaussian 16 program (Revision A.03) with B3LYP functional and 6-31G (d, p) functional. Spin-orbit coupling (SOC) matrix elements between the singlet excited states and triplet excited states were calculated with spin-orbit mean-field (SOMF) methods on ORCA 4.2.1 program with B3LYP functional and def2-TZVP(-f) basis set.

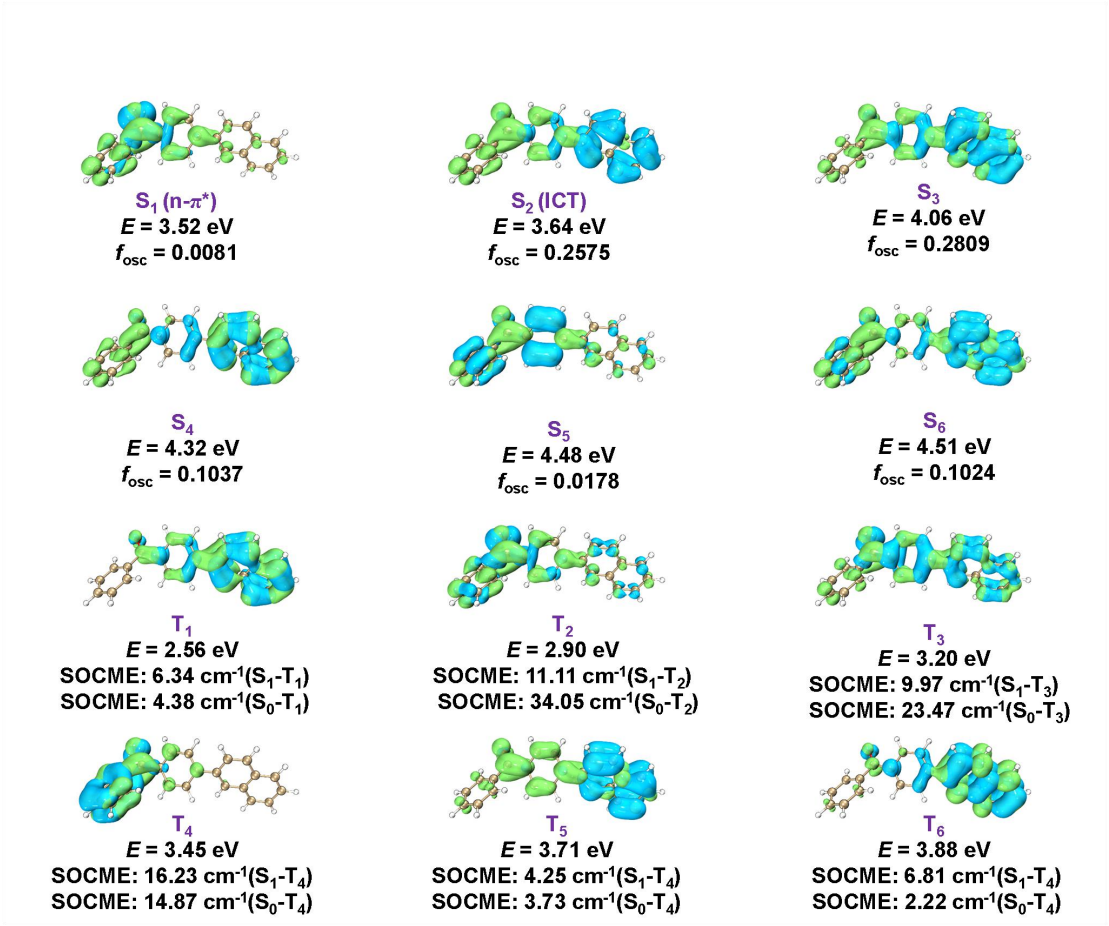

Figure S7. Iso-surface maps of electron-hole density difference of **6**'s S_n and T_n states, where blue and green iso-surfaces correspond to hole and electron distributions, respectively, and SOCME values. The ground-state geometry was optimized by a DFT calculation using B3LYP functional and 6-31G (d, p) basis set. The singlet excited states and triplet excited states were calculated on Gaussian 16 program (Revision A.03) with B3LYP functional and 6-31G (d, p) functional. Spin-orbit coupling (SOC) matrix elements between the singlet excited states and triplet excited states were calculated with spin-orbit mean-field (SOMF) methods on ORCA 4.2.1 program with B3LYP functional and def2-TZVP(-f) basis set.

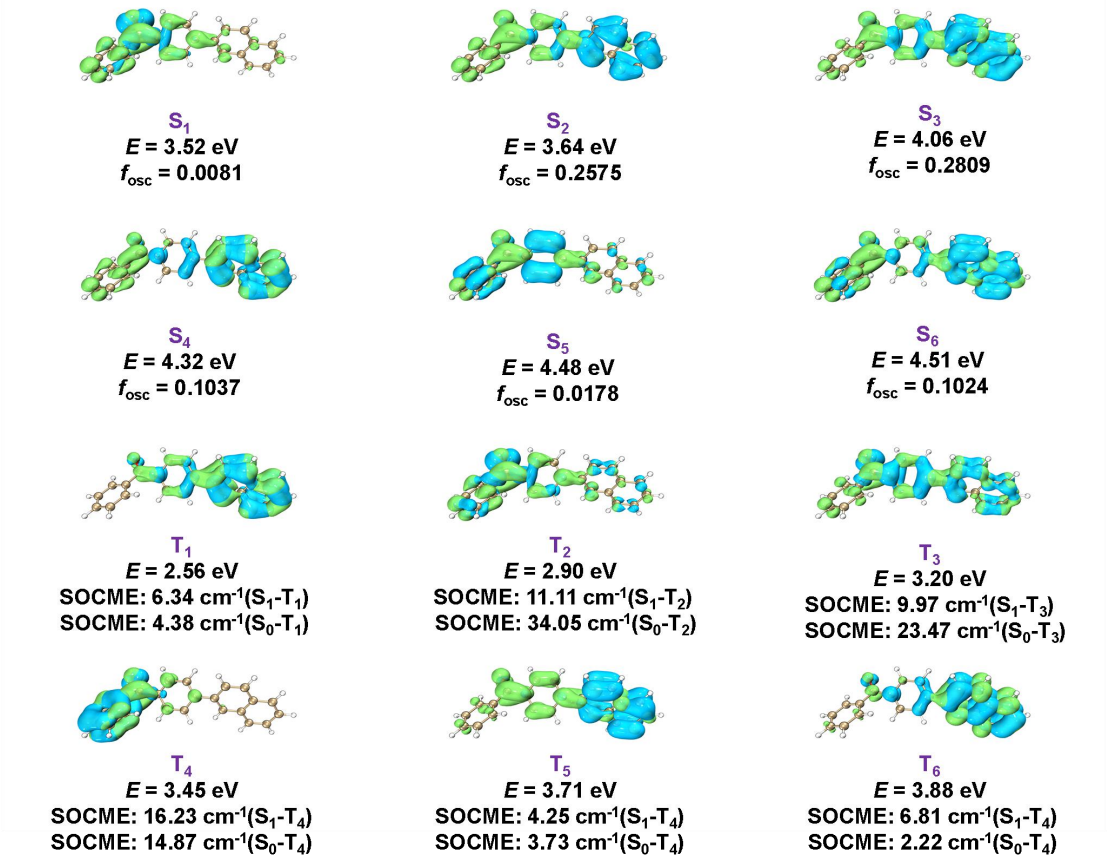

Figure S8. Iso-surface maps of electron-hole density difference of deuterated **6**'s S_n and T_n states, where blue and green iso-surfaces correspond to hole and electron distributions, respectively, and SOCME values. The ground-state geometry was optimized by a DFT calculation using B3LYP functional and 6-31G (d, p) basis set. The singlet excited states and triplet excited states were calculated on Gaussian 16 program (Revision A.03) with B3LYP functional and 6-31G (d, p) functional. Spin-orbit coupling (SOC) matrix elements between the singlet excited states and triplet excited states were calculated with spin-orbit mean-field (SOMF) methods on ORCA 4.2.1 program with B3LYP functional and def2-TZVP(-f) basis set.

Text S1. The photophysical property of deuterated **6**-PhB system.

TD-DFT calculation of D-6 has been performed (Figure S8). It is found that the electron-hole density difference, energy levels and SOCME values are the same before and after deuteration. It should be noted that the significant increase of phosphorescence lifetime of deuterated **6**-PhB under ambient conditions should be attributed to the reduce of nonradiative decay of its triplet excited states, rather than the electronic property of deuterated **6**. It is known that deuteration of RTP molecules can reduce intramolecular motions and nonradiative decay of triplet states;[35-37] the vibration of C-D bonds is much weaker than C-H bonds. Given the phosphorescence lifetime is inversely proportional to $k_P + k_{nr} + k_q$, where k_P, k_{nr} and k_q represent phosphorescence decay constant, nonradiative decay constant and oxygen quenching constant, respectively. The deuteration of compound **6** can significantly reduce k_{nr} and thus increase phosphorescence lifetime of deuterated **6**-PhB under ambient conditions. Fig. 2F shows that two peaks in the range of 410 nm to 470 nm appear at 420 nm and 448 nm in the steady-state emission spectra of deuterated **6**-PhB. In the steady-state emission spectra of **6**-PhB (Fig. 2B), there are emission signals at 420 nm and 448 nm but relatively weak. The deuteration of compound **6** reduces nonradiative decay of both singlet excited states and triplet excited states, leading to the enhancement of emission signals in deuterated **6**-PhB samples. Therefore, it is understandable that the fluorescence maxima in 410-470 nm region become clearly resolved after deuteration and emission enhancement.

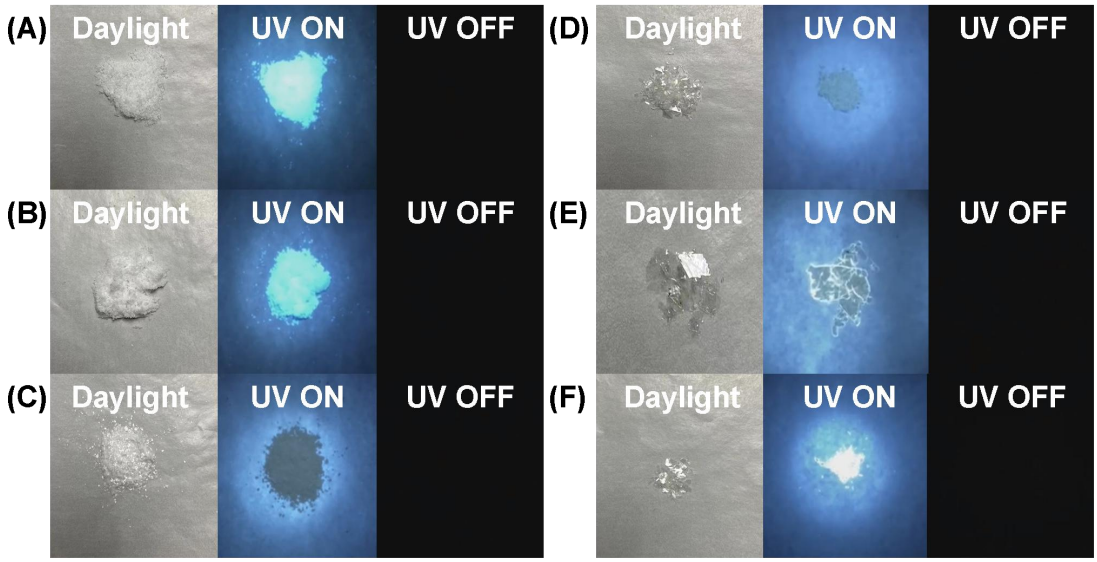

Figure S9. (A) Photographs of compound **1** under daylight, under 365 nm UV lamp, and upon ceasing the 365 nm UV excitation. (B) Photographs of compound **2** under daylight, under 365 nm UV lamp, and upon ceasing the 365 nm UV excitation. (C) Photographs of compound **3** under daylight, under 365 nm UV lamp, and upon ceasing the 365 nm UV excitation. (D) Photographs of compound **4** under daylight, under 365 nm UV lamp, and upon ceasing the 365 nm UV excitation. (E) Photographs of compound **5** under daylight, under 365 nm UV lamp, and upon ceasing the 365 nm UV excitation. (A) Photographs of compound **6** under daylight, under 365 nm UV lamp, and upon ceasing the 365 nm UV excitation.

Table S2. Photophysical data of the (**1**-**6**)-PhB materials under ambient conditions.

Entry	λ_P / nm	τ_P / ms
Compound **1**	427 458 491	0.81 0.80 0.80
Compound **2**	425 452	0.89 0.91
Compound **3**	485 517	179 181
Compound **4**	489 506	291 291
Compound **5**	527 551	288 292
Compound **6**	516 549	956 949

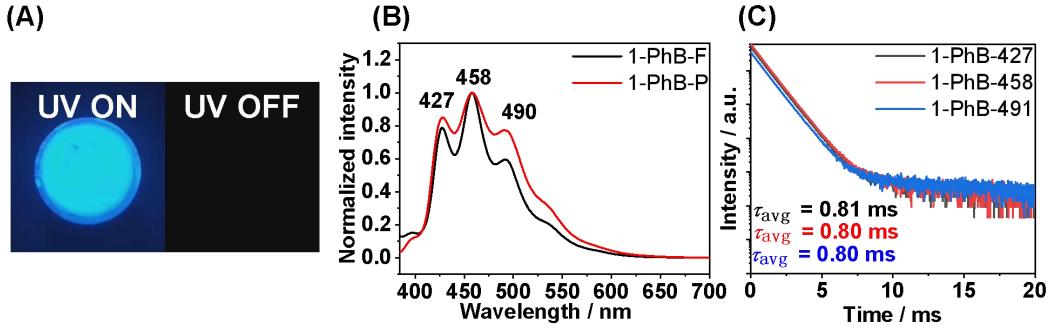

Figure S10. (A) Photographs of **1**-PhB sample obtained under 365 nm UV and after switching-off the UV lamp at room temperature. (B) Room-temperature steady-state and delayed emission (1 ms delay) spectra of **1**-PhB sample. (C) Room-temperature emission decay profile of **1**-PhB sample.

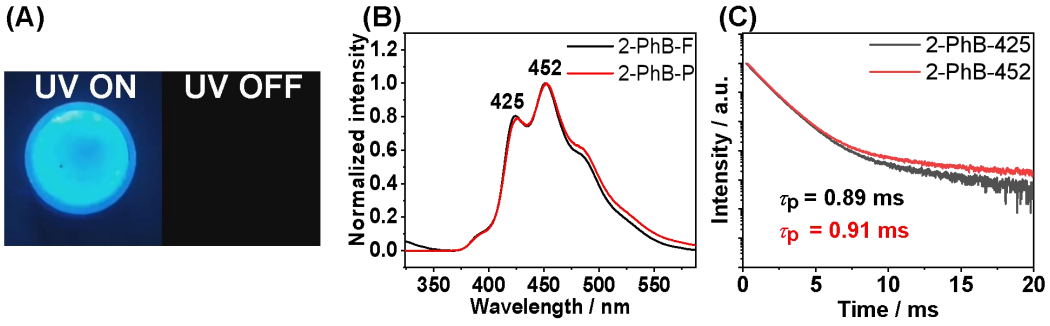

Figure S11. (A) Photographs of **2**-PhB sample obtained under 365 nm UV and after switching-off the UV lamp at room temperature. (B) Room-temperature steady-state and delayed emission (1 ms delay) spectra of **2**-PhB sample. (C) Room-temperature emission decay profile of **2**-PhB sample.

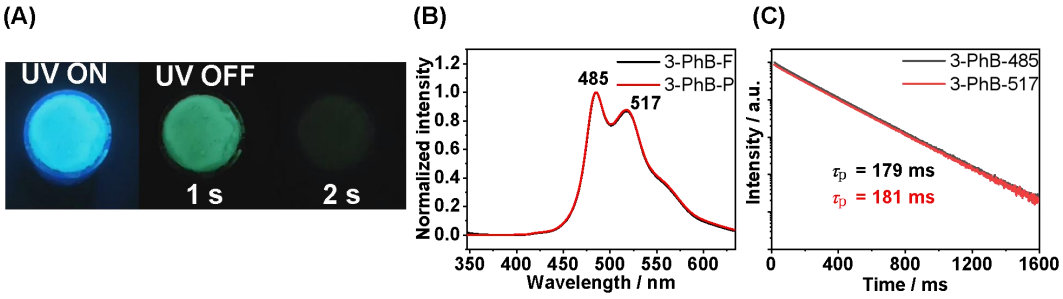

Figure S12. (A) Photographs of **3**-PhB sample obtained under 365 nm UV and after switching-off the UV lamp at room temperature. (B) Room-temperature steady-state

and delayed emission (1 ms delay) spectra of **3**-PhB sample. (C) Room-temperature emission decay profile of **3**-PhB sample.

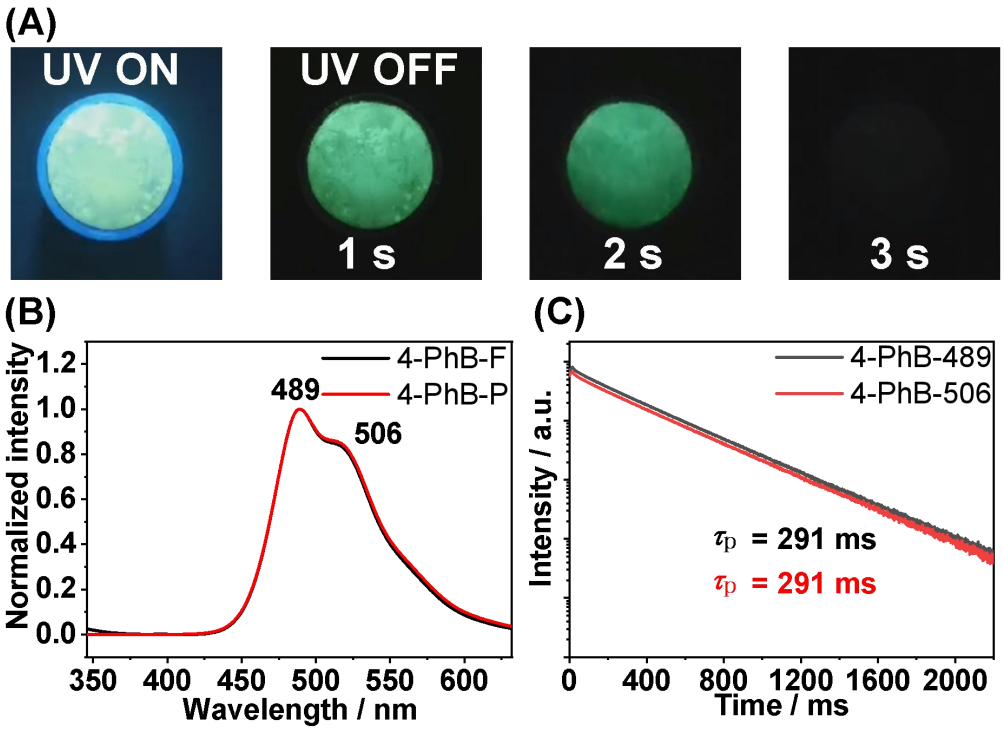

Figure S13. (A) Photographs of **4**-PhB sample obtained under 365 nm UV and after switching-off the UV lamp at room temperature. (B) Room-temperature steady-state and delayed emission (1 ms delay) spectra of **4**-PhB sample. (C) Room-temperature emission decay profile of **4**-PhB sample.

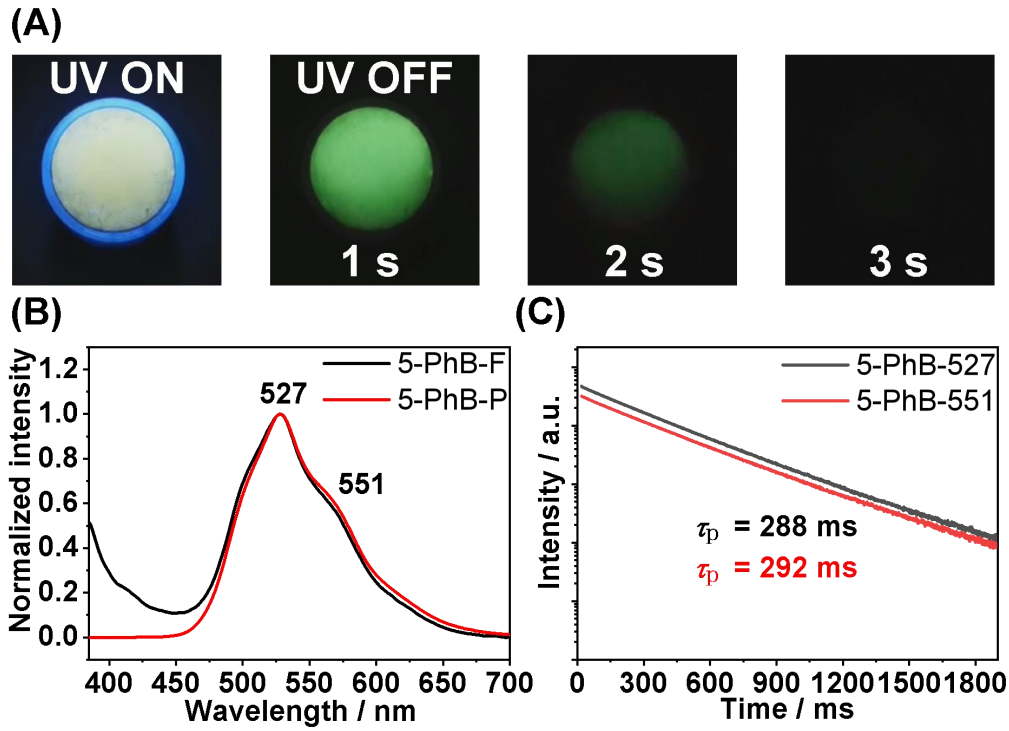

Figure S14. (A) Photographs of **5**-PhB sample obtained under 365 nm UV and after switching-off the UV lamp at room temperature. (B) Room-temperature steady-state and delayed emission (1 ms delay) spectra of **5**-PhB sample. (C) Room-temperature emission decay profile of **5**-PhB sample.

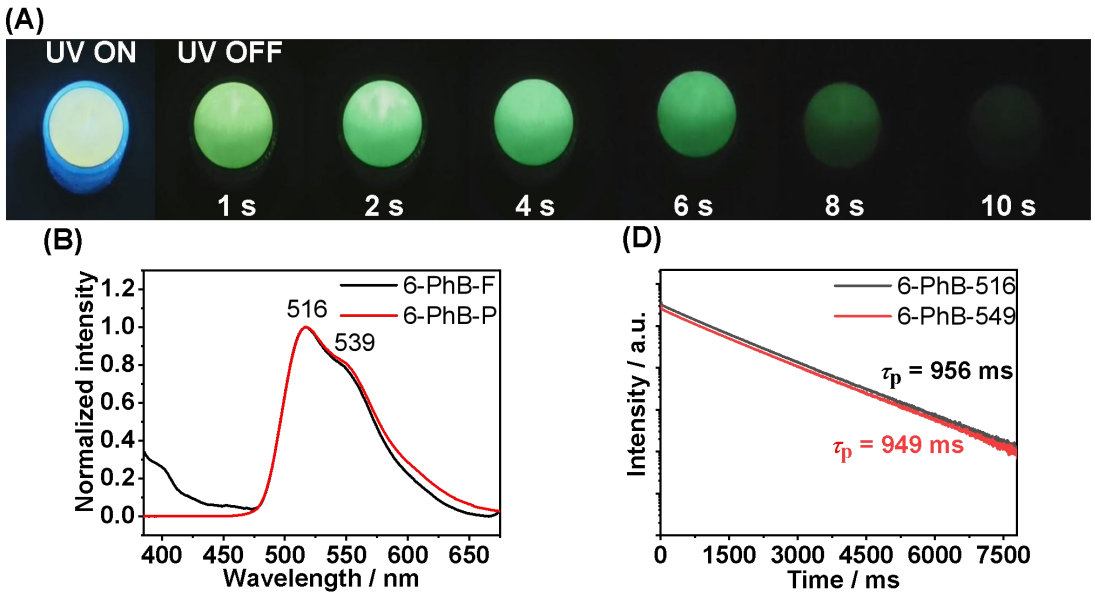

Figure S15. (A) Photographs of **6**-PhB sample obtained under 365 nm UV and after switching-off the UV lamp at room temperature. (B) Room-temperature steady-state

and delayed emission (1 ms delay) spectra of **6**-PhB sample. (C) Room-temperature emission decay profile of **6**-PhB sample.

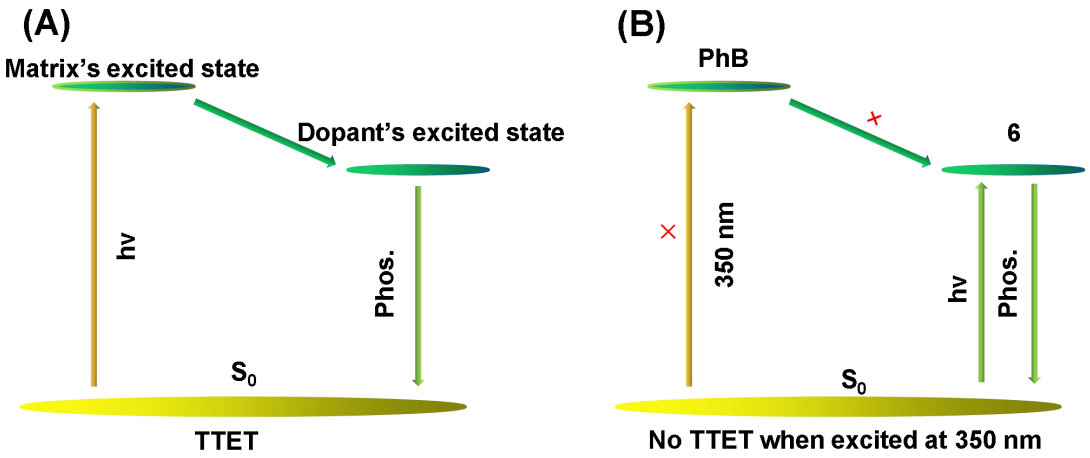

Figure S16. (A) Schematic illustration of triplet-to-triplet excited state energy transfer (TTET) from matrices to dopants in the reported studies. (B) Schematic illustration of the excited state energy levels in the present study. In the reported studies, triplet-to-triplet excited state energy transfer (TTET) from matrices to dopants has been used to assign the RTP mechanism in dopant-matrix systems. It should be noted that significant afterglow properties in these systems can only be observed when the donors were sufficiently excited. In the present study, the afterglow emission of **6**-PhB sample can be excited by 350 nm UV. Since PhB matrices possess negligible UV-vis absorption at 350 nm, the possibility of excited state energy transfer from PhB matrices to compound **6** for the emergence of room-temperature afterglow can be ruled out.

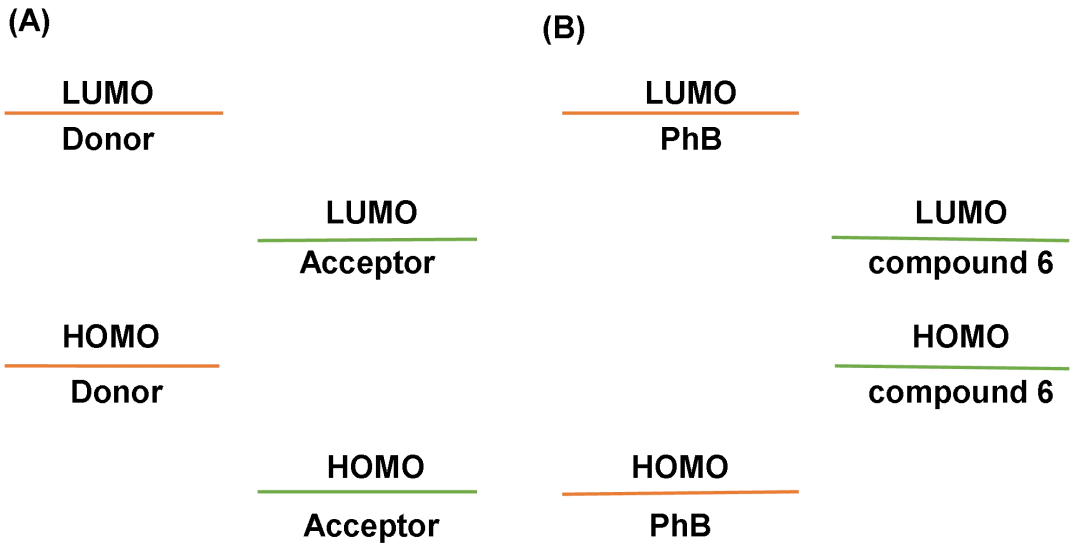

Figure S17. (A) Schematic illustration of HOMO and LUMO levels of donors and acceptors in the organic long persistent luminescence systems with the involvement of intermolecular charge transfer. (B) Schematic illustration of HOMO and LUMO levels of compound **6** and PhB in the present study. In the reported study, photo-induced charge separation and retarded charge recombination can give rise to organic long persistent luminescence with very long afterglow durations at room temperature (*Nature*, 2017, 550, 384). This is not the case in the present study because of the following reasons. First, PhB (HOMO = -6.96 eV, LUMO = -1.79 eV) has lower-lying HOMO and higher-lying LUMO than **6** (HOMO = -5.86 eV, LUMO = -1.84 eV), so intermolecular charge transfer is not likely to occur between **6** and PhB. Second, UV-vis spectra of **6**-PhB solids are difficult to collect. The excitation spectra of **6**-PhB can reflect the UV-vis absorption property of **6**-PhB sample. It is found that the excitation spectra of **6**-PhB sample (Figure S20C) have similar shape and maxima to the UV-vis spectra of **6** solutions (Figure S20B), which also suggest the absence of intermolecular charge transfer between **6** and PhB. Third, the steady-state emission bands of intermolecular charge transfer system are usually broad and structureless. In contrast, the steady-state emission bands of **6**-PhB sample have structures (Fig. 2B). Forth, the organic long persistent luminescence usually follows power law decay in the excited state decay profile, whereas the excited state decay profile of **6**-PhB sample follows single-exponential decay. These, together with the significant

localized excitation (LE) character of naphthalene group and small n-π* character of benzophenone group in **6**'s T_1 state, indicate the long afterglow duration of **6**-PhB materials is originated from room-temperature phosphorescence.

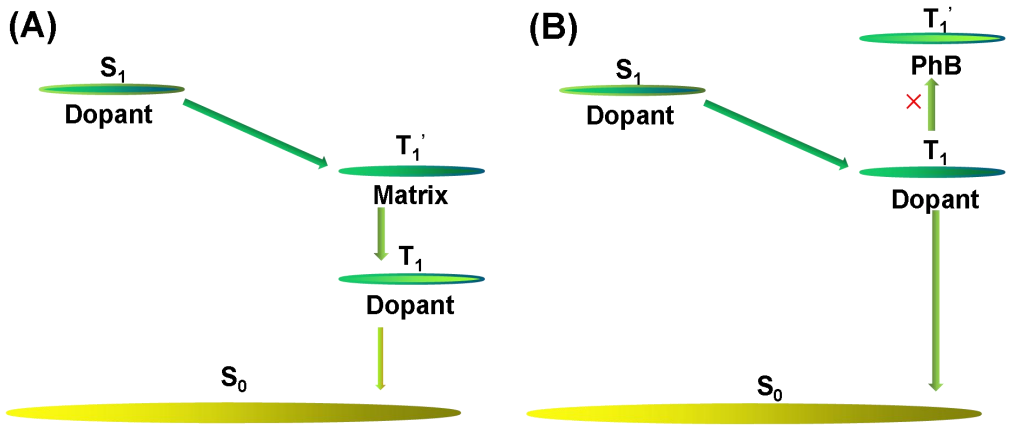

Figure S18. (A) Schematic illustration of the enhancement of intersystem crossing mediated by matrices' T_1 states. (B) Excited state energy levels of dopants and matrices in the present study. Recent studies in the literature showed that triplet excited states of organic matrices with energy levels sandwiched between S_1 and T_1 states of phosphorescence dopants can mediate singlet-to-triplet ISC of the phosphorescence dopants, leading to the emergence of room-temperature afterglow. This mediation of ISC by matrices' T_1 states is not the case in the present **6**-PhB system since T_1 level of PhB matrices is much higher than both **6**'s S_1 and T_1 levels. Actually, according to the studies by Adachi's group and us, high T_1 levels of organic matrices are very important for the fabrication of high-performance afterglow materials since it can avoid afterglow quenching caused by triplet-to-triplet energy transfer from luminescent dopants to organic matrices.

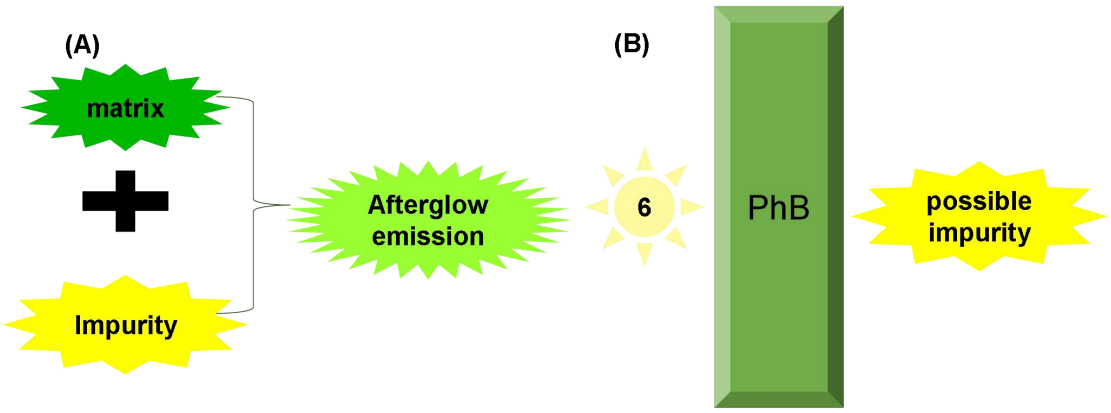

Figure S19. (A) Schematic illustration of the impurity mechanism for organic afterglow. (B) Schematic illustration of the separation of compound **6** and possible impurity by PhB matrices in the present study. Recent studies showed that isomeric impurity can lead to organic afterglow in carbazole systems. In the present study, compound **6** was carefully purified by column chromatography followed by two cycles of recrystallization in spectroscopic grade dichloromethane/n-hexane; HPLC also confirms the high purity. Charge separation and charge recombination processes which are essential for organic afterglow are statistically negligible.

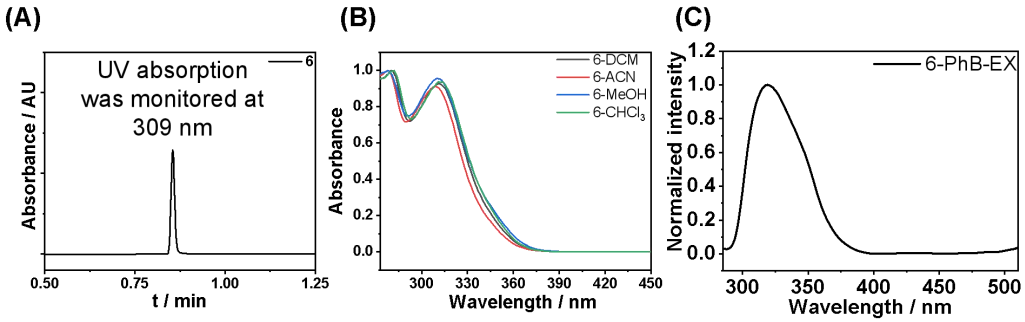

Figure S20. (A) HPLC profile of compound **6**. UV absorption was monitored at 309 (B) UV-vis spectra of compound **6** in different solvents. DCM, ACN, MeOH and $CHCl_3$ refer to dichloromethane, acetonitrile, methanol and chloroform, respectively. (C) Excitation spectra of **6**-PhB samples.

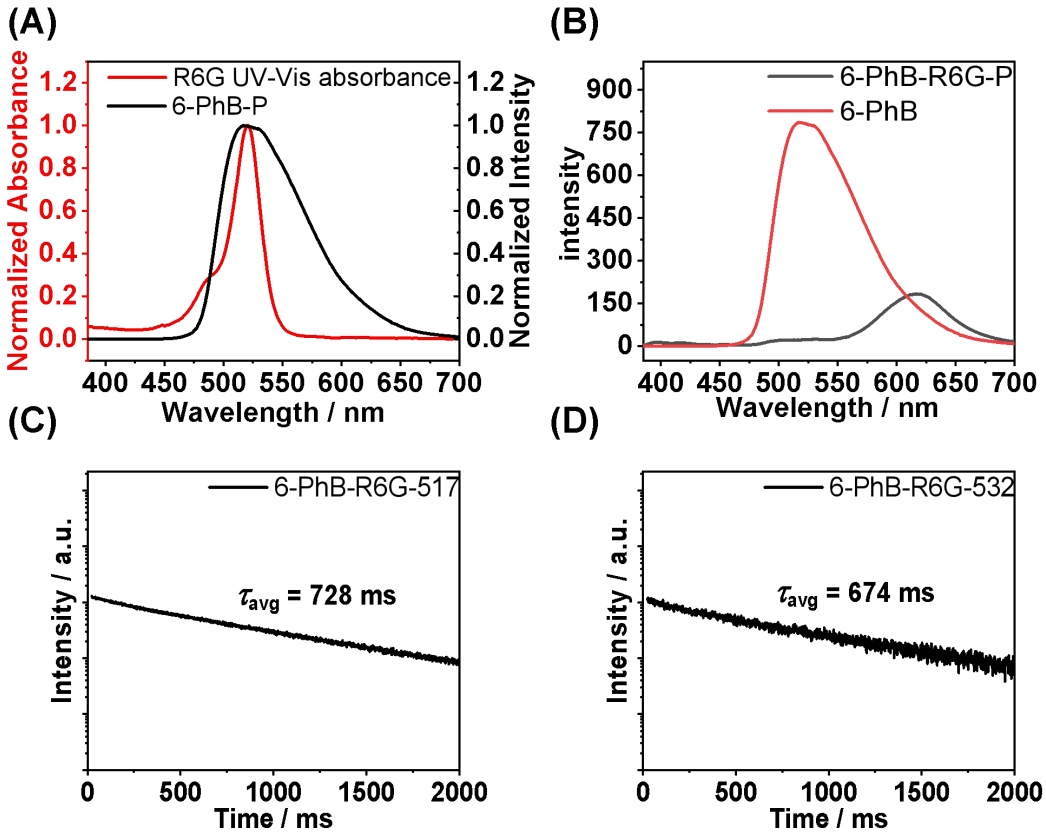

Figure S21. (A) Normalized UV-vis spectra of R6G (red line) and normalized delayed emission spectra of **6**-PhB materials (black line). (B) Delayed emission spectra of **6**-PhB materials (red line) and **6**-PhB-R6G materials (black line). (C, D) Room-temperature afterglow decay of **6**-PhB-R6G materials monitored at 517 nm (C) and 532 nm (D). It is found that the delayed emission intensity of compound **6** in PhB (470-550 nm region) shows significant decrease after adding R6G into **6**-PhB system. It is also found that the delayed emission lifetimes of compound **6** in PhB decrease after adding R6G into **6**-PhB system. These, together with the emergence of red afterglow (Fig. 4E) and the donor-acceptor spectral overlap, indicate the energy transfer from **6** to R6G in PhB matrix.

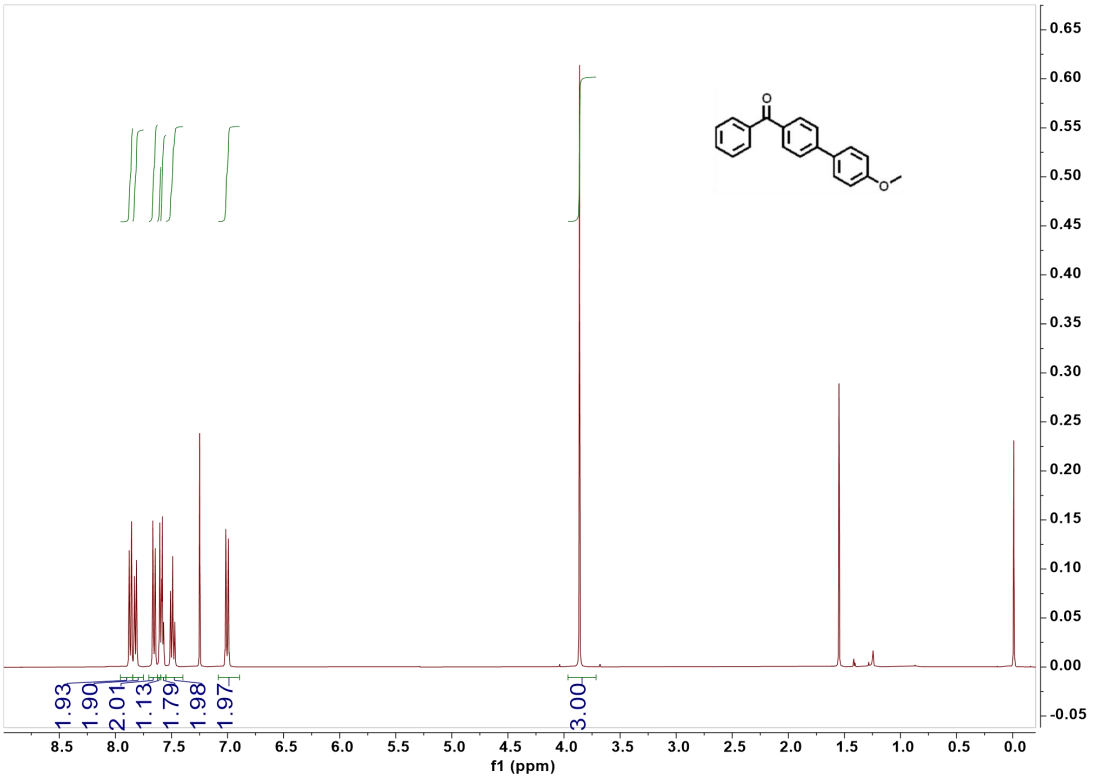

Figure S22. ^{1}H NMR spectra of compound **4**.

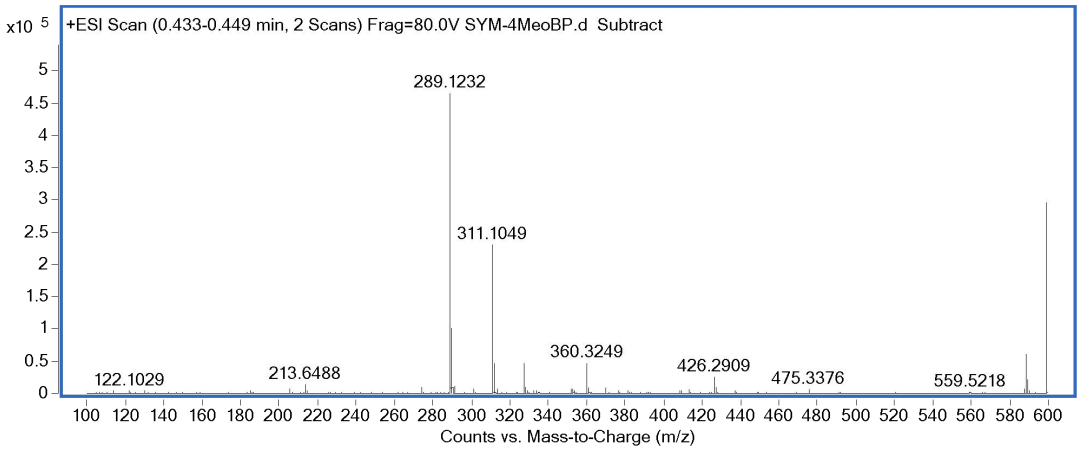

Figure S23. HRMS spectra of compound **4**.

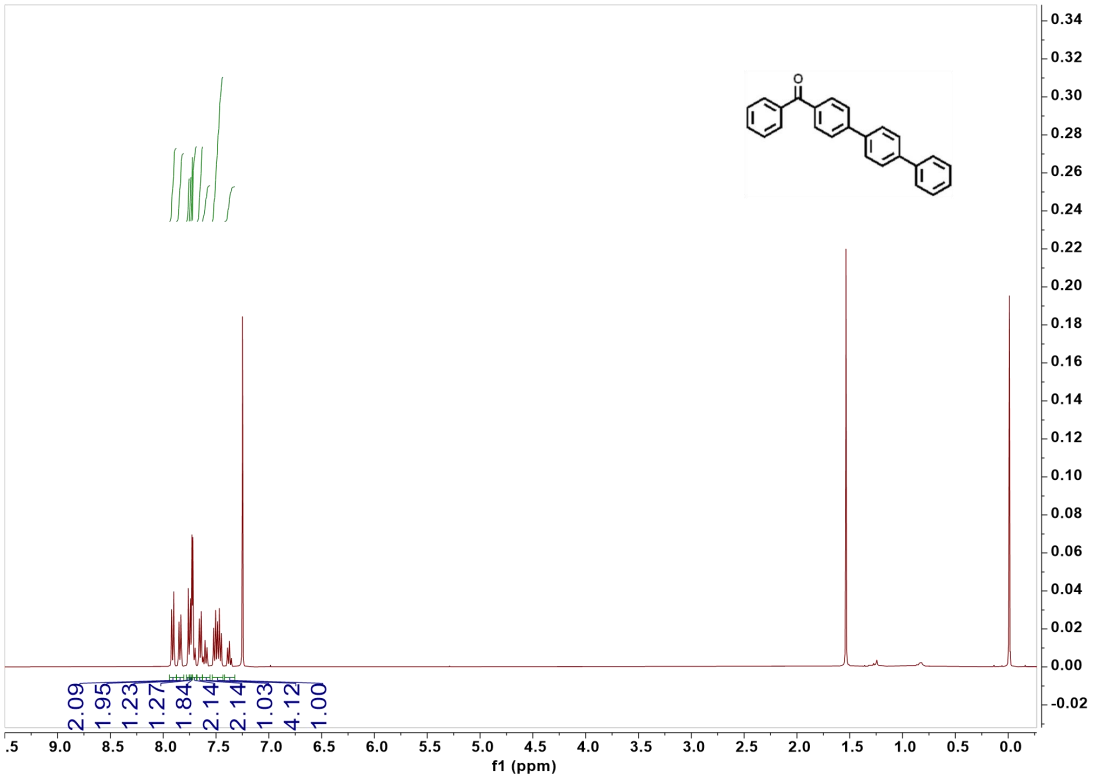

Figure S24. [1]H NMR spectra of compound **5**.

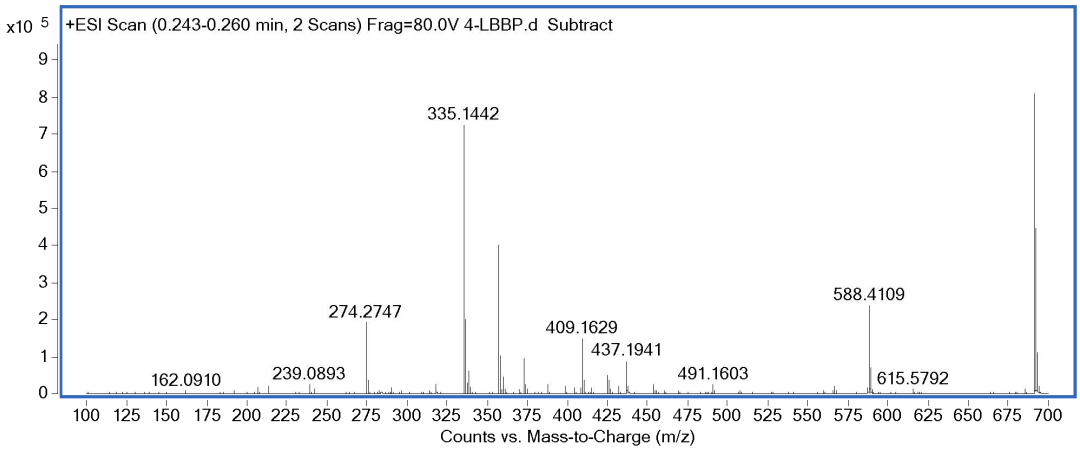

Figure S25. HRMS spectra of compound **5**.

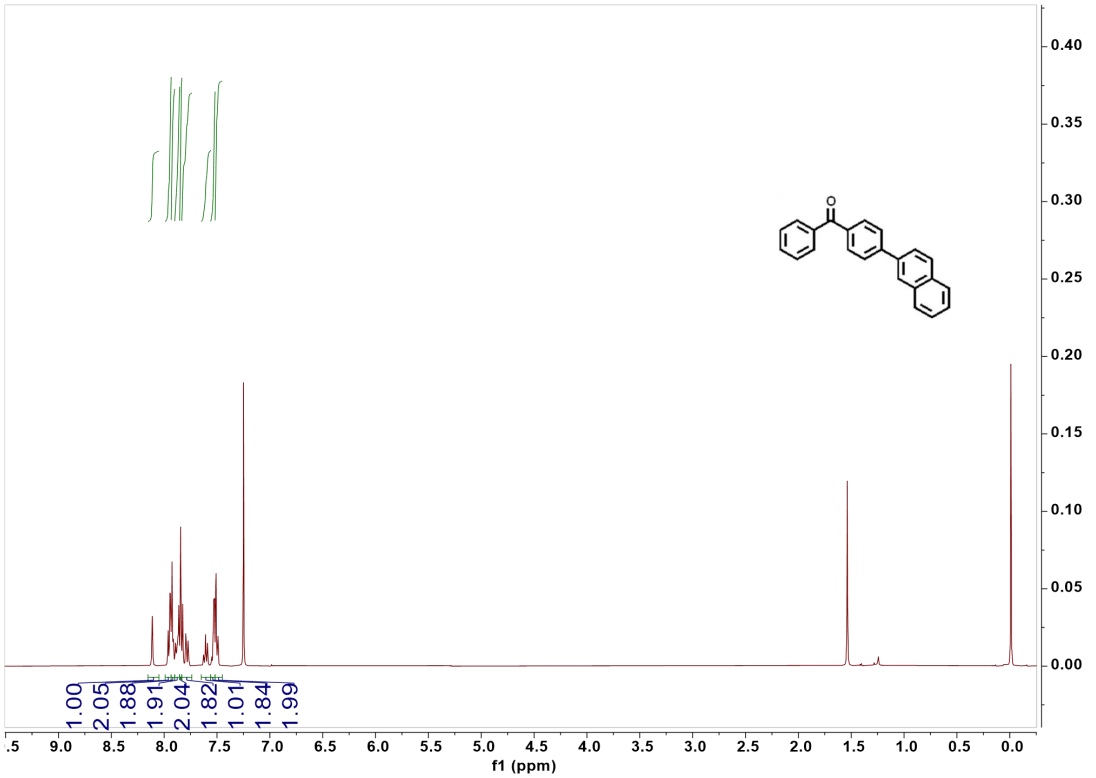

Figure S26. [1]H NMR spectra of compound **6**.

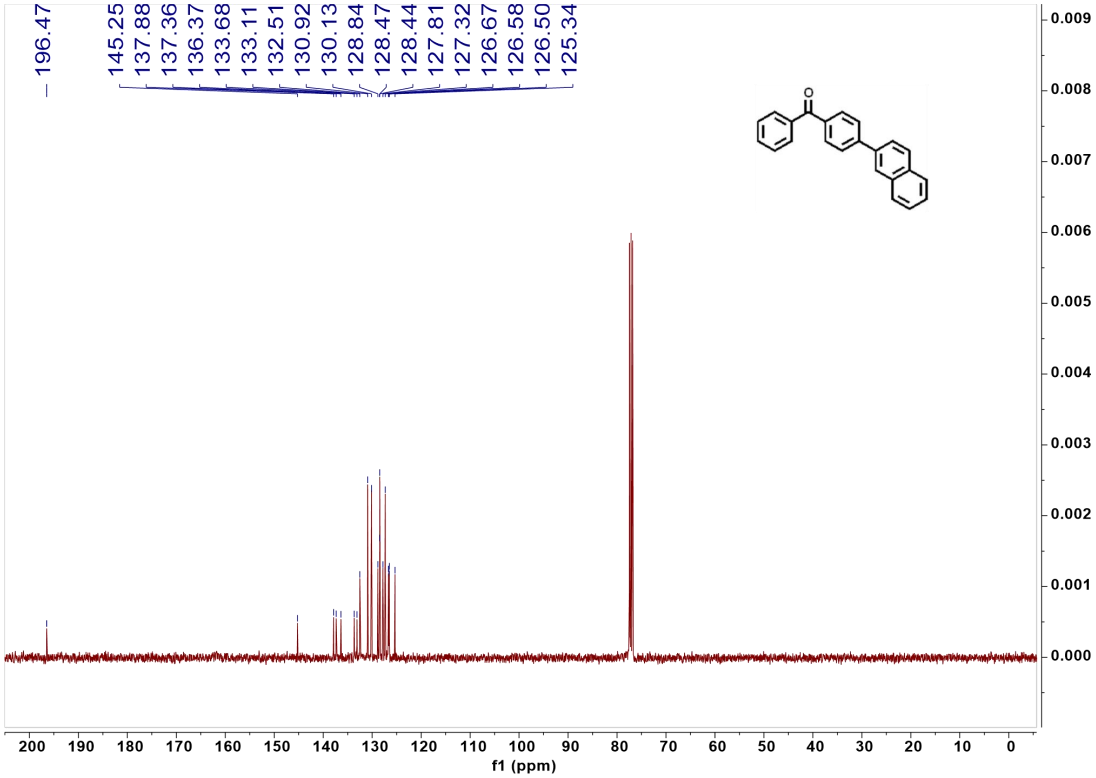

Figure S27. [13]C NMR spectra of compound **6**.

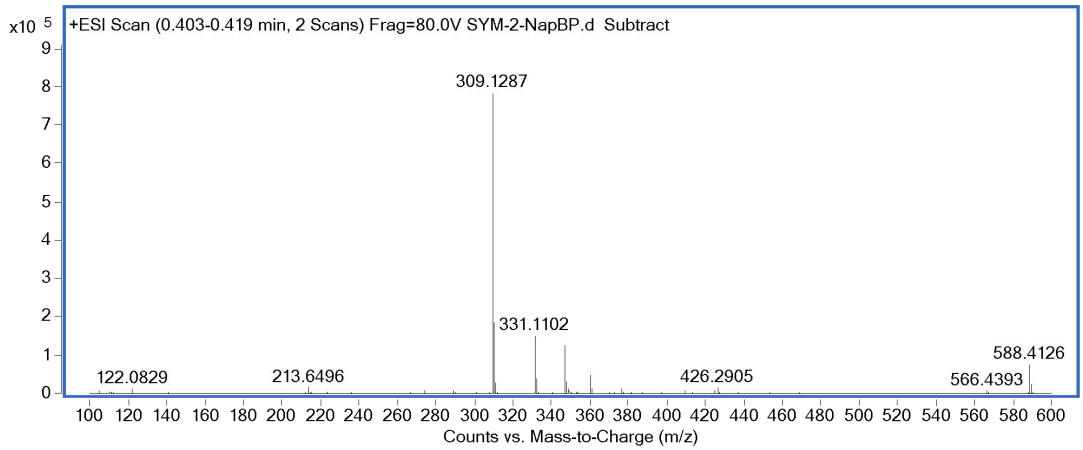

Figure S28. HRMS spectra of compound **6**.

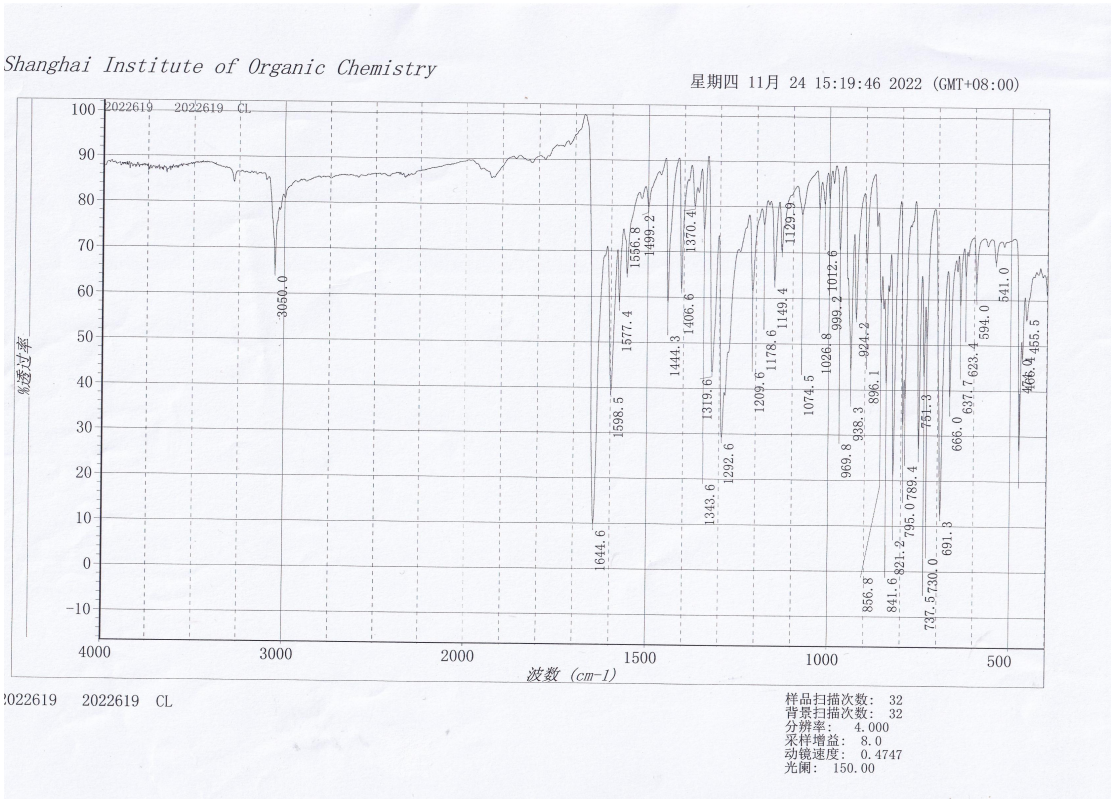

Figure S29. FT-IR spectra of compound **6**.